ADVANCED FUNCTIONAL MATERIALS
www.afm-journal.de

Surface-Decorated High-Entropy Alloy Catalysts with Significantly Boosted Activity and Stability

Kaizhu Zeng, Jianwei Zhang, Wenqiang Gao, Lianping Wu, Hanwen Liu, Jinlong Gao, Zezhou Li, Jihan Zhou, Teng Li, Zhiqiang Liang, Bingjun Xu,* and Yonggang Yao**

High-entropy alloy (HEA) nanoparticles are emerging catalytic materials and are particularly attractive for multi-step reactions due to their diverse active sites and multielement tunability. However, their design and optimization often involve lengthy efforts due to the vast multielement space and unidentified active sites. Herein, surface decoration of HEA nanoparticles to drastically improve the overall activity, stability, and reduce cost is reported. A two-step process is employed to first synthesize non-noble HEA (FeCoNiSn) nanoparticles and then are surface alloyed with Pd (main active site), denoted as NHEA@NHEA-Pd. As a demonstration in the ethanol oxidation reaction, a high mass activity of 7.34 A mg^{-1}_{Pd} and superior stability (>91.8% retention after 2000 cycles) in NHEA@NHEA-Pd are achieved, substantially outperforming traditional HEA, binary M@M-Pd (M = Sn, Fe, Co, Ni), and commercial Pd/C. In situ spectroscopy reveals that NHEA@NHEA-Pd can catalytically produce and oxidize CO at <0.5 V, which is >200 mV lower than Sn@Sn-Pd, suggesting enhanced activity in NHEA@NHEA-Pd owing to Pd's unique high-entropy coordination environment. This work provides a novel design of HEA catalysts by combining surface decoration (exposing more active sites) and high-entropy coordination (enhancing intrinsic activity and structural stability) to boost catalysts' activity and durability.

1. Introduction

High-entropy alloy (HEA) nanoparticles, composed of multiple elements (usually four or more) arranged in a single solid-solution phase, have attracted increasing attention for catalysis due to their tunable catalytic properties, strong multielement synergy, and high-entropy stabilization.[1–6] The use of multiple elements significantly broadens the compositional space and affords tunable microstructures to achieve high performance. It is reported that HEA catalysts are featured with complex atomic configurations and diverse adsorption sites, which result in a near-continuous distribution in binding energy[7–9] that is well-suited for multi-step reactions having a wide range of intermediates.[10] Meanwhile, the high-entropy structure usually leads to the excellent structural stability of HEA catalysts, either through the thermodynamic entropy stabilization effect or kinetic sluggish diffusion,[11–20] thus promoting their applications in harsh environments. Indeed, HEA catalysts have demonstrated high activity and excellent stability in various thermo- and electrocatalytic applications, such as ammonia oxidation[6] and decomposition,[14,21] water splitting,[10,22–24] carbon dioxide (CO_2) reduction,[25,26] methanol oxidation,[27] ethanol oxidation[28,29] and other reactions.[30–32]

Despite the considerable promise, the rational design of HEA catalysts remains challenging owing to the almost unlimited compositional space and the lack of understanding of the structure-activity correlations, hindering their rapid exploration.[7,14,33–35] The complex composition and distribution of the multitude of elements in the HEA are reported to substantially

K. Zeng, H. Liu, J. Gao, Y. Yao
State Key Laboratory of Materials Processing and Die & Mould Technology
School of Materials Science and Engineering
Huazhong University of Science and Technology
Wuhan 430074, P. R. China
E-mail: yaoyg@hust.edu.cn

J. Zhang, Z. Liang
Institute of Functional Nano and Soft Materials (FUNSOM) and Jiangsu Key Laboratory for Carbon-Based Functional Materials and Devices
Soochow University
Suzhou 215123, P. R. China
E-mail: zqliang@suda.edu.cn

W. Gao, Z. Li, J. Zhou, B. Xu
Beijing National Laboratory for Molecular Sciences
College of Chemistry and Molecular Engineering
Peking University
Beijing 100871, P. R. China
E-mail: b_xu@pku.edu.cn

L. Wu, T. Li
Department of Mechanical Engineering
University of Maryland
College Park, MD 20742, USA

The ORCID identification number(s) for the author(s) of this article can be found under https://doi.org/10.1002/adfm.202204643.

DOI: 10.1002/adfm.202204643

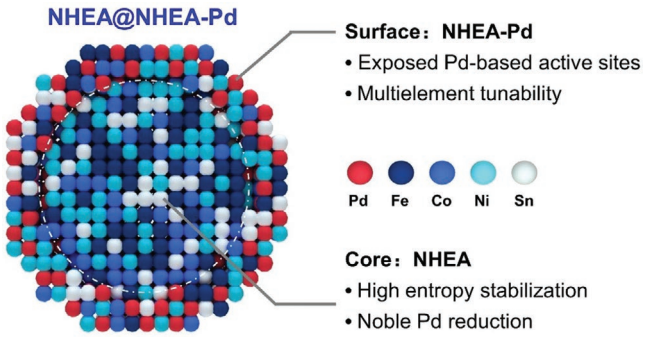

Scheme 1. The scheme of NHEA@NHEA-Pd catalyst. NHEA@NHEA-Pd is composed of the inner core FeCoNiSn and the outer shell decorated with Pd-based active sites. The surface decoration of Pd exposes the most active sites and significantly reduces the catalyst cost, while multielement composition provides wide tunability and multifunctionality for efficient catalysis.

affect the catalytic activity mainly through the ligand effect, that is, synergy from the random spatial distribution of different metal elements.[36,37] In addition, most HEA catalysts are based on extremely non-equilibrium synthesis (e.g., 2000 K, 55 ms) to enable homogeneous mixing.[3,6,35,38–42] Such a homogeneous structure limits structural flexibility and particularly noble metal usage since most noble metal atoms are located inside HEA nanoparticles. To improve the atom efficiency and accelerate the development of HEA catalysts, a few well-established synthetic strategies in conventional catalyst design could be adopted:[7,43,44] i) increasing the surface area by introducing highly porous and/or hierarchical structures, such as core-shell structures, octahedral frames, nanocages, and nanowires,[45–54] and ii) enhancing the intrinsic activity of active sites by tuning the local coordination environment of active elements including doping and alloying, geometric and morphological control (size, shape, facets), and nanoparticle-support interactions.[7,43,55–61]

Despite tremendous efforts dedicated to the synthesis and compositional optimization of HEAs, the structural and morphological design of HEA catalysts is relatively under-explored, mainly owing to the challenges of balancing the extreme synthesis conditions and delicate controls of the HEA surface. Herein, we report surface-decorated HEA catalysts composed of non-noble HEA as the core (FeCoNiSn, denoted as NHEA) and surface alloyed with Pd to form NHEA@NHEA-Pd (**Scheme 1**). Such a design highlights the critical importance of selectively exposing Pd-based active sites at the surface while retaining the ability to modulate Pd's activity via the unique high-entropy coordination environment (FeCoNiSn) toward highly efficient and durable catalysts. In the current context, the high-entropy coordination environment refers to the random spatial distribution of various non-noble metal elements (FeCoNiSn) surrounding the catalytically active site, that is, Pd. The FeCoNiSn elements were chosen owing to their low cost and easy accessibility. They were also frequently reported for alloying with noble metals to achieve efficient catalysts.[28,62]

We used ethanol oxidation reaction (EOR), the anode reaction in the direct ethanol fuel cell,[63–65] as a model reaction to demonstrate the utility of surface-decorated HEA catalysts. Ethanol oxidation to CO_2 and H_2O is a complex multi-electron transfer process involving dissociative adsorption, C-H and C-C bond activation, as well as carbon monoxide (CO) oxidation,[66–68] which is an ideal model reaction to test the effectiveness of our HEA design. Indeed, NHEA@NHEA-Pd exhibited a high mass activity of 7.34 A mg^{-1}_{Pd}, excellent stability (>91.8% retention after 2000 cycles), and enhanced CO tolerance, indicating the critical role of high-entropy coordination and morphological control in HEA catalysts toward improved activity, stability, as well as significantly reduced cost.

2. Results and Discussion

2.1. Synthesis and Characterizations of NHEA@NHEA-Pd Nanocatalysts

Figure 1a schematically shows the synthesis process of NHEA@NHEA-Pd. First, the precursor solution (0.05 mol L^{-1}) composed of various non-noble metal salts (i.e., Fe, Co, Ni, Sn) in an equimolar ratio was mixed with carbon black, where the total metal loading is 8 wt%. After drying, the mixture was evenly spread on a carbon cloth heating element for rapid radiative Joule heating.[69] We then used a two-step heating process to separately synthesize solid-solution NHEA (FeCoNiSn) alloy and Pd-decorated alloy surface to achieve NHEA@NHEA-Pd (Figure 1b). The first heating features a high temperature with a long duration (i.e., 1750 K for 1 s), which is designed to induce multielement mixing for the single-phase formation of non-noble NHEA. After this high-temperature shock, we added the noble Pd salt solution into as-prepared NHEA nanoparticles and then performed the second heating at a lower temperature with a shorter duration (i.e., 1118 K for 0.3 s) to form NHEA@NHEA-Pd. The lower temperature and shorter duration synthesis are designed to ensure Pd metal atoms, mostly decorated on the surface of NHEA by limiting atom diffusion.[6]

Figure 1c shows the X-ray diffraction (XRD) patterns of NHEA and NHEA@NHEA-Pd. After the first-step high-temperature shock synthesis, the NHEA sample illustrates a clear face-centered-cubic (FCC) structure with distinct diffraction peaks attributed to (111), (200), and (220) planes, indicating a single-phase structure. Meanwhile, the NHEA@NHEA-Pd remains a single-phase FCC structure without an obvious Pd phase (PDF No. 89–4897), which may come from the ultrasmall size of Pd decorated on NHEA. Figure 1d,e demonstrates the morphologies of carbon-supported NHEA@NHEA-Pd nanoparticles taken at different magnifications. 50 mg NHEA@NHEA-Pd catalysts were collected in a vial after one-batch synthesis (Figure 1d), suggesting that gram-scale catalyst production could be achieved in minutes. These NHEA@NHEA-Pd nanoparticles with an average diameter of ≈25 nm were uniformly dispersed on carbon black (Figure 1e and Figure S1, Supporting Information). We also performed X-ray photoelectron spectroscopy (XPS) characterization for NHEA@NHEA-Pd. As shown in Figure S2, Supporting Information, the deconvoluted Pd 3d spectrum (Pd $3d_{5/2}$ and Pd $3d_{3/2}$) suggests that the Pd is in a metallic state.

From the high-resolution transmission electron microscope (HRTEM) image (Figure 1f), the atomic structure of NHEA@NHEA-Pd also suggests the formation of a single-phase FCC, in which the distance between adjacent lattice fringes is 2.04 Å,

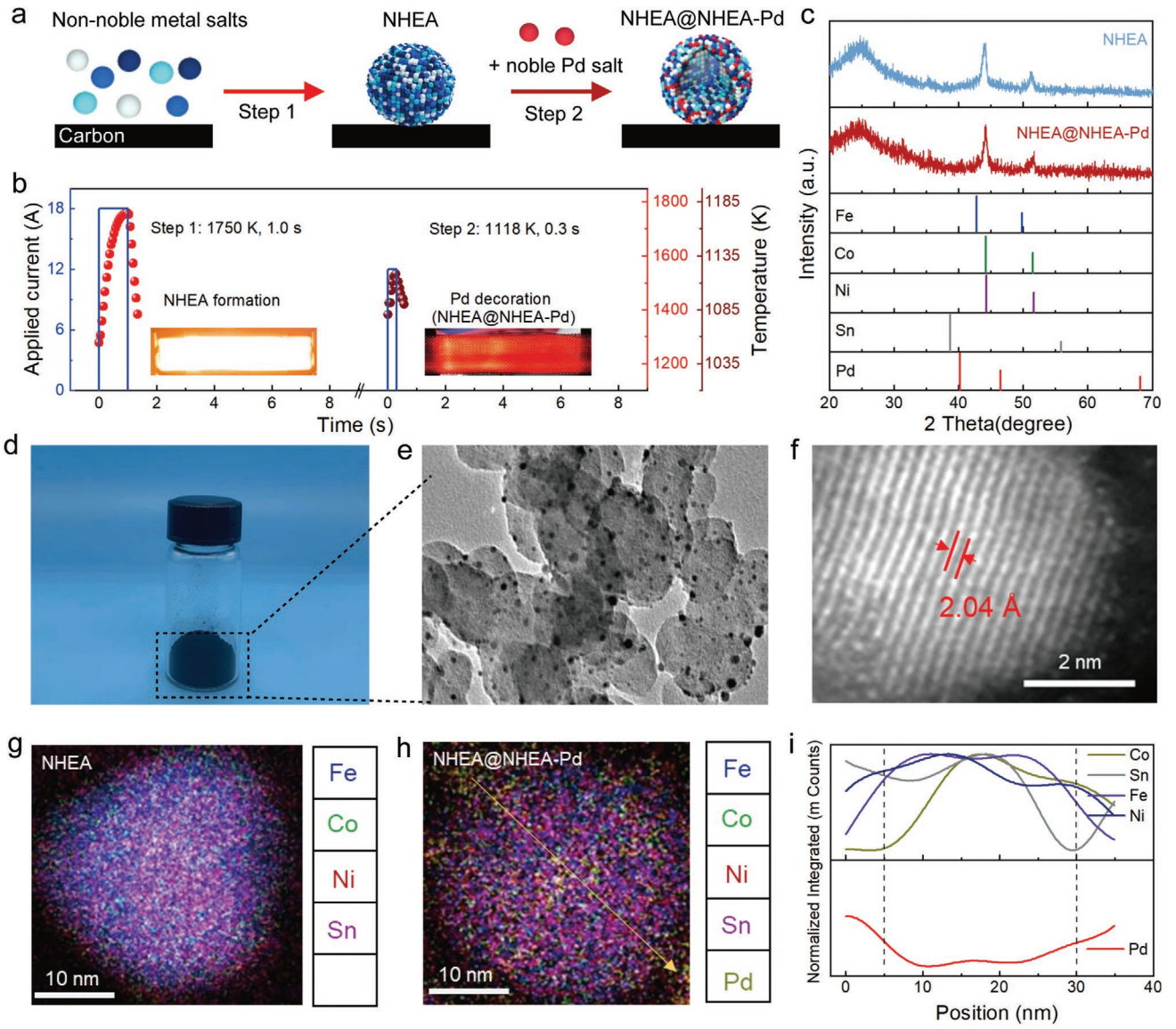

Figure 1. Synthesis of carbon-supported NHEA@NHEA-Pd catalysts using two-step thermal shock method. a) Schematic for the synthesis of NHEA@NHEA-Pd nanoparticles supported on a carbon substrate. b) The temperature profiles used in the two-step thermal shock synthesis and corresponding optical images. c) XRD patterns of NHEA and NHEA@NHEA-Pd supported on carbon. d) Photograph of carbon-supported NHEA@NHEA-Pd catalysts (50 mg). e) TEM image for NHEA@NHEA-Pd nanoparticles uniformly dispersed on carbon black. f) HRTEM image for NHEA@NHEA-Pd, revealing the single-phase FCC structure and Pd atoms distributed on the NHEA surface. g) Elemental mapping image of NHEA, showing the homogenous mixing of all elements. h) Elemental mapping image of NHEA@NHEA-Pd and i) the line scan signals of Fe, Co, Ni, Sn, and Pd across the NHEA@NHEA-Pd nanoparticle, suggesting the Pd element dispersed mostly on the surface of solid-solution FeCoNiSn alloy.

which can be indexed to the *d* spacing of the (111) of FCC Co (PDF NO. 15-0806). There are also many bright dots on the nanoparticle, which indicates dispersed Pd atoms (with larger atomic weight) on the NHEA surface. The elemental mapping of Figure 1g shows the homogeneous distribution of the four non-noble metal components throughout the NHEA nanoparticle after the first-step high-temperature synthesis. Then, by adding the Pd precursor into the as-prepared NHEA and performing the second-step heating, Pd metals are well dispersed on the NHEA surface, as revealed by the elemental mapping and its corresponding line scan signals where Pd atoms are mostly distributed on the surface of nanoparticles (Figure 1h,i). These results confirm the synthesis of surface-decorated HEAs and the critical role of two-step heating in achieving multielement mixing and surface decoration.

2.2. Structural Modulation of Pd Dispersion in NHEA Catalysts

Compared with solid-solution HEAs, NHEA@NHEA-Pd with surface decoration significantly reduces the fraction of noble metal embedded inside nanoparticles, which could

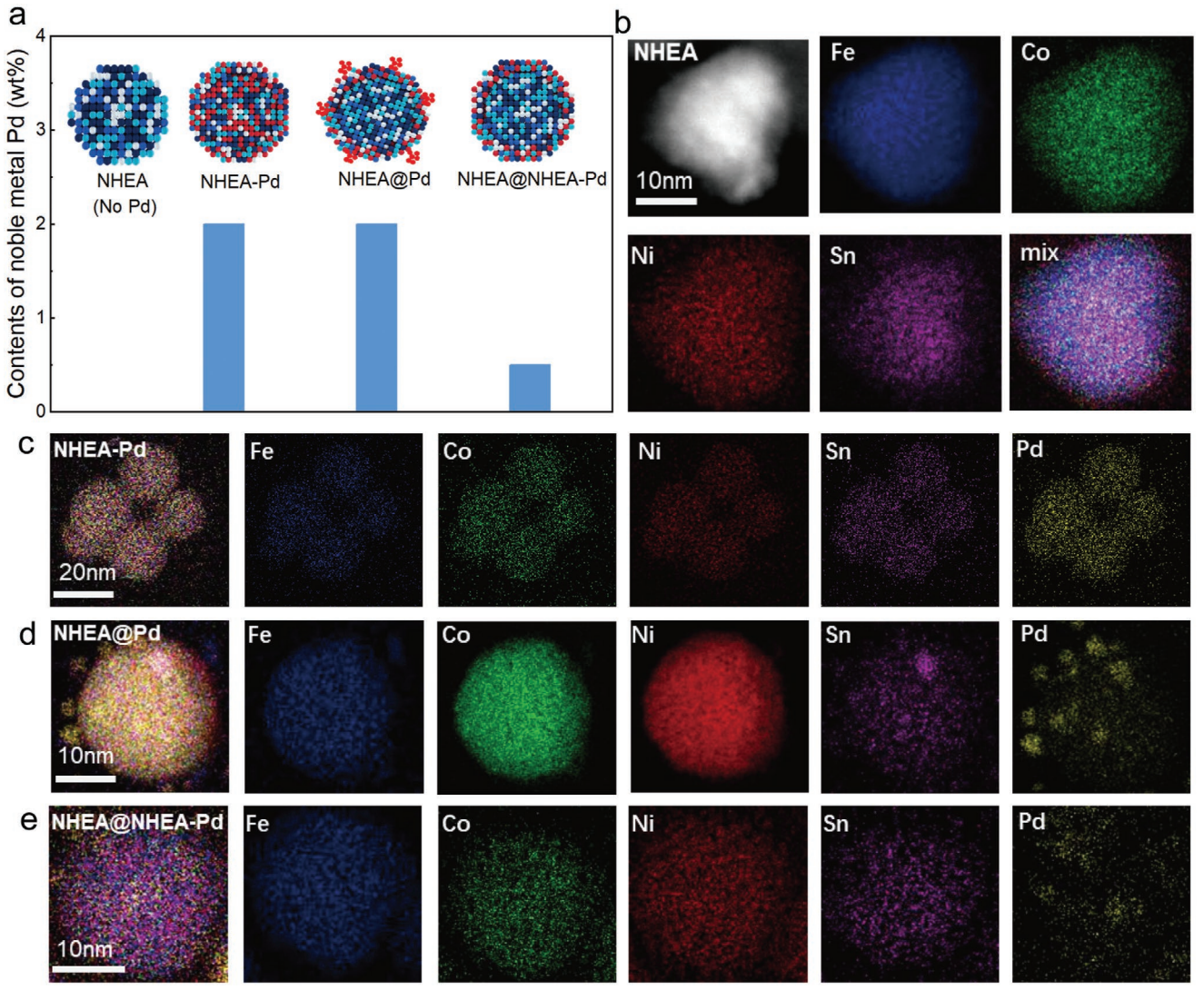

Figure 2. Structural modulation of Pd dispersion in NHEA catalysts. a) Schematic images of four HEA catalysts with different Pd loading and dispersion. Detailed elemental mappings of b) NHEA (one-step shock synthesis), c) NHEA-Pd (one-step shock synthesis), d) NHEA@Pd (two-step shock synthesis), and e) NHEA@NHEA-Pd (two-step shock synthesis, reduced Pd loading), demonstrating the successful control of Pd dispersion on the NHEA surface by designing thermal shock process and optimizing Pd loading.

substantially lower the cost without sacrificing performance. Here we deliberately design and tailor the synthesis processing, temperature profile, and the content of the noble element as shown in Figure S3, Supporting Information, to show the synthesis condition as well as the resulting structures. In the following four HEAs, including: 1) one-step synthesized pure NHEA (FeCoNiSn) without Pd, 2) one-step synthesized solid-solution NHEA-Pd (FeCoNiSnPd), 3) two-step synthesized NHEA@Pd with a high Pd loading (≈2 wt% in the metal alloy), and 4) NHEA@NHEA-Pd with low Pd loading (≈0.5 wt% in the metal alloy) (**Figure 2**a). For NHEA without Pd addition, Fe, Co, Ni, and Sn elements were homogenously mixed into a single phase revealed by its elemental mappings (Figure 2b) and XRD (Figure 1c). Similarly, NHEA-Pd prepared by one-step shock synthesis displays uniform mixing and distribution of Pd to form the HEA structure (Figure 2c and Figure S4a,b, Supporting Information), which is verified by its XRD result (Figure S5a, Supporting Information). The XRD shows a single-phase FCC, and its diffraction peaks move towards low angles compared with that of NHEA because of the introduction of Pd with a large atomic radius (1.37 Å).

In contrast, the two-step thermal shock method leads to the formation of heterogeneous HEAs, which is more evident when the amount of Pd is higher in NHEA@Pd (Figure S4c,d, Supporting Information), where the Pd clusters are decorated mostly on the NHEA surface (Figure 2d). The XRD result also shows the coexistence of the metallic Pd and the FCC phase in NHEA@Pd (Figure S5b, Supporting Information). By substantially reducing the Pd loading (i.e., in NHEA@NHEA-Pd), Pd is almost atomically dispersed on the NHEA surface with few remained clusters (Figure 2e). This suggests that a higher loading of Pd leads to the formation of Pd clusters while a lower loading induces the near-atomic dispersion of Pd on the NHEA surface, which forms a high-entropy coordination environment.

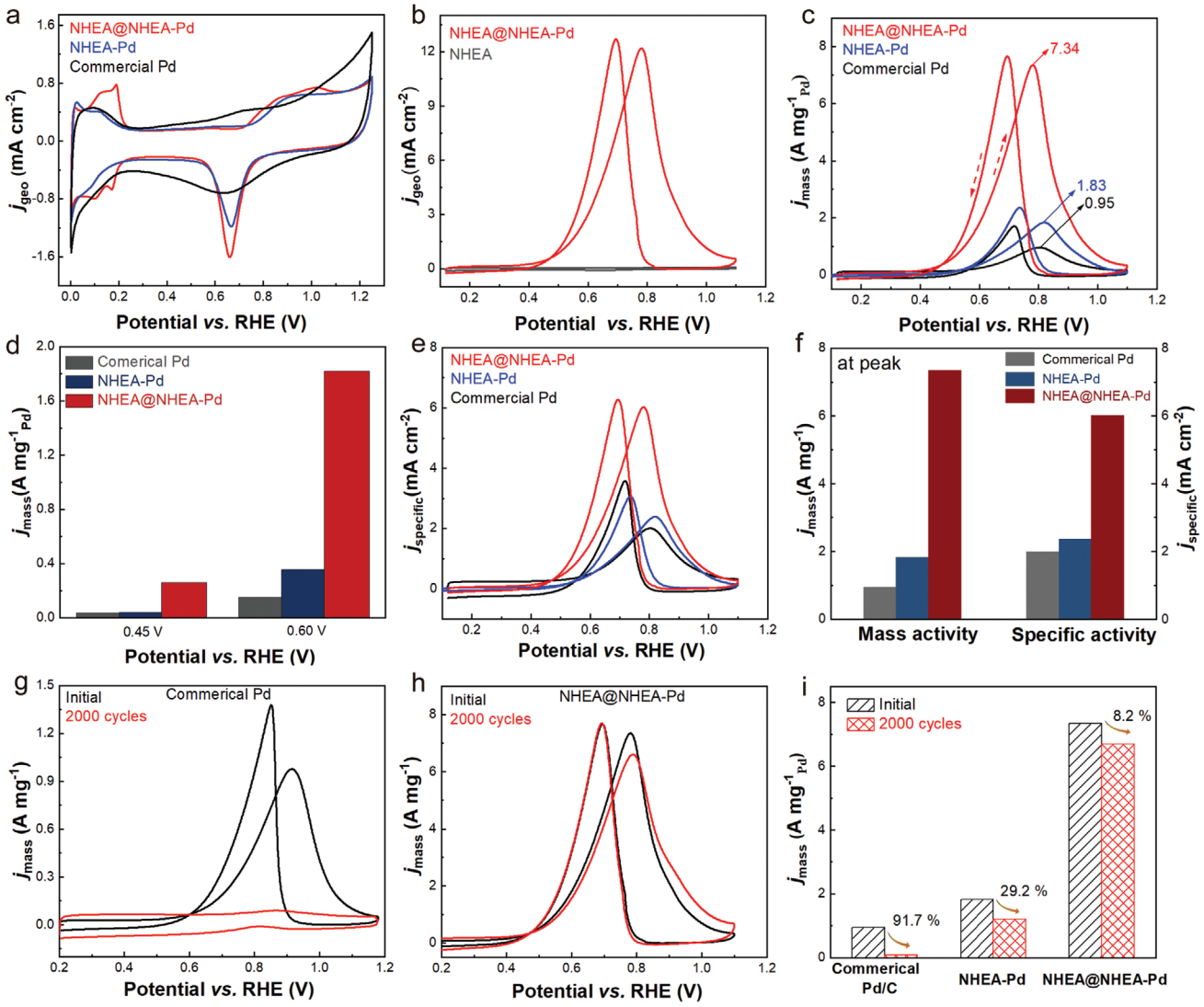

Figure 3. Electrochemical EOR measurements of NHEA@NHEA-Pd. a) CV measurements of NHEA@NHEA-Pd, NHEA-Pd, and commercial Pd in N_2-saturated 0.5 M H_2SO_4 solution at a scan rate of 20 mV s^{-1}. b) Geometric activities of NHEA@NHEA-Pd and NHEA for EOR in N_2-saturated aqueous solution containing 1.0 M KOH and 1.0 M ethanol at a scan rate of 20 mV s^{-1}. c) Mass activities of NHEA@NHEA-Pd, NHEA-Pd, and commercial Pd for EOR and d) j_{mass} values at 0.45 and 0.60 V in the forward scan. e) $j_{specific}$ values of NHEA@NHEA-Pd, NHEA-Pd, and commercial Pd normalized by the ECSAs. f) The mass activities and specific activities of NHEA@NHEA-Pd, NHEA-Pd, and commercial Pd at their peak current density. g–i) Comparison of the stability of NHEA@NHEA-Pd, NHEA-Pd, and commercial Pd for EOR after 2000 cycles.

The two-step heating, therefore, plays a critical role in synthesizing surface-decorated HEA.

Highly dispersed Pd atoms on the NHEA surface can enhance atom utilization efficiency and expose more Pd-based active sites, leading to boosted catalysis performance. Therefore, by adjusting the thermal shock process and Pd loading, we can tune the Pd dispersion in/on the NHEA and achieve structural modulation in NHEA@NHEA-Pd for highly efficient catalysis. We test the EOR performance of NHEA@Pd and NHEA@NHEA-Pd (Figure S6a, Supporting Information). Here NHEA@NHEA-Pd shows better EOR performance as compared to NHEA@Pd at 0.60 V (Figure S6b, Supporting Information), indicating the importance of Pd incorporation and a high-entropy coordination environment for enhancing the activity.

2.3. NHEA@NHEA-Pd in Catalysis

We compared the EOR activity of different catalysts by both mass activity and specific activity, where the current is normalized by the noble metal mass (A mg$^{-1}_{Pd}$) or the electrochemically active surface area (ECSA, mA cm^{-2}) of each catalyst. **Figure 3**a illustrates the normalized cyclic voltammetry (CV) curves of these catalysts in a 0.5 M H_2SO_4 solution with the scan rate of 20 mV s^{-1} from 0.05 to 1.20 V (vs reversible hydrogen electrode [RHE]). The voltammograms exhibit well-established features of adsorption and desorption of the H species on Pd sites. However, it is known that the hydrogen adsorption method is less reliable for ECSA[70] assessment of Pd-based electrocatalysts due to the formation of bulk Pd hydride.[71] Instead, the

Table 1. Comparison of different catalysts for the EOR performance.

Catalysts	$ECSA_{PdO}$ [$m^2\ g^{-1}_{Pd}$]	j_{mass} [A mg^{-1}_{Pd}]	$j_{specific}$ [mA cm^{-2}]	E_{onset} [V]	Method
NHEA@NHEA-Pd	94.41	7.34	6.20	0.37	Two-step
NHEA-Pd	77.45	1.83	2.38	0.42	One-step
Commercial Pd	27.94	0.95	2.07	0.57	N/A
Sn@Sn-Pd	32.96	1.26	3.95	0.44	Two-step
Co@Co-Pd	30.76	0.23	1.58	0.52	Two-step
Fe@Fe-Pd	24.69	0.22	1.14	0.60	Two-step
Ni@Ni-Pd	24.92	0.14	0.46	0.63	Two-step

ECSAs of these catalysts were evaluated by determining the Coulombic charge associated with the reduction peak of the Pd oxidation layer on the surface during the negative CV scan at ≈0.71 V versus RHE, as summarized in **Table 1**. The ECSA of NHEA@NHEA-Pd is 94.43 $m^2\ g^{-1}_{pd,}$ higher than NHEA-Pd (77.15 $m^2\ g^{-1}_{pd}$) and commercial Pd (27.94 $m^2\ g^{-1}_{pd}$) (Figure S7, Supporting Information). This is due to the majority of Pd atoms in NHEA@NHEA-Pd being exposed to the reactive surface by our surface decoration and two-step synthesis. Thus, the formation of HEA and a hybrid structure could greatly increase the ECSA and the utilization efficiency of Pd. In addition, there might be different active sites for the different steps in the cascade reactions. For example, the initial reaction might proceed at a Pd-based site and the consecutive reaction might occur at a non-noble metal-based site.[19]

The electrocatalytic performance of these samples toward EOR was tested in 1.0 M KOH + 1.0 M ethanol solution at the scan rate of 20 mV s^{-1}. Two characteristic oxidation peaks were observed from CV curves, in which the peak in the forward scan was associated with ethanol oxidation, while the peak in the reverse scan originated from further oxidation or removal of the poisoning carbonaceous intermediate. First, we compared the performance of NHEA and NHEA@NHEA-Pd. As shown in Figure 3b, NHEA did not promote the EOR, due to the absence of an obvious ethanol oxidation peak (<0.1 mA cm^{-2}), suggesting that NHEA is not active toward EOR. In contrast, the NHEA@NHEA-Pd shows excellent EOR performance with a high current density of 12.05 mA cm^{-2}, indicating that the high activity comes from the Pd surface decoration. Although NHEA alone shows negligible activity compared to the NHEA@NHEA-Pd, this does not mean that NHEA contributes negligibly to EOR; in fact, the NHEA structure in NHEA@NHEA-Pd should be critical for promoting the cascade reactions and contribute to the high activity in NHEA@NHEA-Pd, as we showed later when compared with pure Pd or Sn@Sn-Pd with different coordination environments.

We also compared the EOR activity of different Pd-contained catalysts: NHEA@NHEA-Pd, NHEA-Pd, and commercial Pd. Both their mass activities (normalized to the mass of Pd) and specific activities (normalized to the ECSA) were recorded as shown in Figure 3c–e. NHEA@NHEA-Pd shows the highest mass activity (j_{mass}) and specific activities ($j_{specific}$). In detail, the forward anodic current density reaches 7.34 A mg^{-1}_{Pd}, which is 4.01- and 7.48-fold that of NHEA-Pd (1.83 A mg^{-1}_{Pd}) and commercial Pd (0.98 A mg^{-1}_{Pd}), respectively. We further compared the j_{mass} at 0.45 and 0.60 V in the forward anodic current density (Figure 3d). NHEA@NHEA-Pd is 6.5 and 6.6 times (at 0.45 V) and 5.1 and 12.1 times (at 0.60 V) more active than the NHEA-Pd and commercial Pd, respectively. The catalytic activity and stability of our NHEA@NHEA-Pd are comparable to the reported catalysts[29,72–75] (Figure S8, Supporting Information).

To eliminate the size effect and active site exposure differences, we also normalized the activities by the ECSA to obtain the specific activity. Still, NHEA@NHEA-Pd shows better performance (6.2 mA cm^{-2}) than NHEA-Pd and commercial Pd (Figure 3e,f). The improved mass activity and specific activity in NHEA@NHEA-Pd indicates not only more exposed active sites by surface decoration but also enhanced intrinsic activity of Pd interaction with NHEA, which we will discuss later. In addition, the onset potential (defined as the potential at 5% of the peak current density) of NHEA@NHEA-Pd is ≈0.37 V, which is more negative than those of NHEA-Pd (≈0.42 V) and commercial Pd (≈0.58 V) (Table 1). This suggests that the NHEA@NHEA-Pd with surface decoration can quickly react on the catalyst surface at a low potential, and thus high intrinsic activity.

The stability of NHEA@NHEA-Pd in EOR was examined by continuous CV scans in the ethanol-containing electrolyte. As shown in Figure 3g, commercial Pd sharply decrease in activity by 91.7% after 2000 cycles, which may be due to easy CO poison and catalysts aggregation in commercial Pd/C.[76] In contrast, NHEA@NHEA-Pd shows little change (8.2%) in the CV curves after 2000 cycles, while the mass activity of NHEA-Pd reduces by ≈29.2% after 2000 cycles (Figure 3h and Figure S9, Supporting Information). Figure 3i summarizes the activity changes of Pd, NHEA-Pd, and NHEA@NHEA-Pd before and after cycling. Compared with single-element Pd, both NHEA-Pd and NHEA@NHEA-Pd show improved stability due to their high-entropy structure featuring an entropy-stabilization effect. Also, our high-temperature synthesis (either one-step or two-step method) ensures the interfacial stability between alloys and carbon substrate, avoiding catalyst agglomeration and thus enhancing catalysis stability.[77] Note that NHEA@NHEA-Pd exhibits better stability than NHEA-Pd, which may result from that NHEA@NHEA-Pd has a higher Pd content at the surface to stabilize the structure, while Pd in the NHEA-Pd is diluted throughout the particles, resulting in less Pd at the surface. In addition, chronoamperometry (CA) at 0.45 V was adopted as another method to evaluate the stability of NHEA@NHEA-Pd (Figure S10, Supporting Information). The steady current density of NHEA@NHEA-Pd was 1.5 and 6.25 times higher than that of NHEA-Pd and commercial Pd, respectively.

We also used post-mortem analysis by XRD and TEM to reveal the stability performance of NHEA@NHEA-Pd after cycling. As shown in Figure S11a, Supporting Information, the NHEA@NHEA-Pd catalyst remains the FCC structure the same as the one before cycling, suggesting structural stability which may come from the entropy stabilization. In addition, NHEA@NHEA-Pd nanoparticles were also uniformly dispersed on the carbon black substrate without obviously nanoparticle aggregation after cycling (Figure S11b, Supporting Information). This reveals that the catalyst has high interfacial stability between the nanoparticles and the carbon substrate, benefiting from our high-temperature synthesis method with strong interfacial adhesion, as reported in the literature.[20] Therefore, the surface-decorated NHEA catalyst not only reduces the amount of noble metal used but also improves its activity and stability, illustrating the effectiveness of hybrid high-entropy design in enhancing structural stability and catalytic performance.

2.4. Origin of High Performance in the NHEA@NHEA-Pd Catalyst

To demonstrate the critical role of the high-entropy coordination environment in the EOR performance, we compared individual metal M@M-Pd (M = Sn, Fe, Co, Ni) with NHEA@NHEA-Pd. As shown in Figure S12, Supporting Information, the nanoparticles show a uniform distribution on carbon black with a similar morphology feature. In addition, we have also carried out the XRD characterization for M@M-Pd (Figure S13, Supporting Information). The ECSAs of these catalysts were calculated based on the charge required for the Pd oxide reduction (Table 1 and Figure S14, Supporting Information). From **Figure 4**a,b, the specific activity of NHEA@NHEA-Pd (6.2 mA cm^{-2}) surpasses that of Sn@Sn-Pd (3.97 mA cm^{-2}), Co@Co-Pd (1.57 mA cm^{-2}), Fe@Fe-Pd (0.45 mA cm^{-2}), and Ni@Ni-Pd (1.15 mA cm^{-2}), respectively. These results imply the largely enhanced intrinsic activity in NHEA@NHEA-Pd.[77] Figure S15, Supporting Information, shows the mass activity where NHEA@NHEA-Pd (7.34 A mg^{-1}_{Pd}) has the highest j_{mass} than Sn@Sn-Pd (1.26 A mg^{-1}_{Pd}), Co@Co-Pd (0.23 A mg^{-1}_{Pd}), Fe@Fe-Pd (0.24 A mg^{-1}_{Pd}), and Ni@Ni-Pd (0.14 A mg^{-1}_{Pd}), respectively. Importantly, even the sum of their mass activities (1.85 A mg^{-1}_{Pd}) is still lower than NHEA@NHEA-Pd. We also tested the stability of Sn@Sn-Pd (the highest activity among the M@M-Pd). As shown in Figure S16, Supporting Information, after 2000 cycles, the activity of Sn@Sn-Pd decreases by 86.5%. These results suggest that the NHEA coordinated Pd plays a critical role in affecting the activity and stability of Pd-based active sites, potentially through the multielement synergy and ligand effects as reported in many alloys and core-shell catalysts.[78–80]

We carried out CO stripping experiments in the saturated CO solution of 1.0 M KOH to explore the CO tolerance on our studied catalysts. As shown in Figure 4c and Figure S17, Supporting Information, the NHEA@NHEA-Pd catalyst shows a CO oxidation peak at 0.79 V, which is 30–150 mV more negative in comparison to that on Sn@Sn-Pd (0.86 V), Fe@Fe-Pd (0.89 V), Co@Co-Pd (0.88 V), Ni@Ni-Pd (0.94 V), and commercial Pd (0.88 V), suggesting better catalytic CO oxidation/removing capability and therefore, higher activity (early reaction) and stability (anti-CO poison). In addition, a consecutive CV scan for all samples was tested in a normal electrolyte (1.0 M KOH without CO), and the CO oxidation peak is absent, indicating the complete elimination of CO on the catalyst surface (Figures S18 and S19, Supporting Information). The results indicate excellent catalytic CO oxidation and superior CO tolerance on NHEA@NHEA-Pd.

Moreover, we employed in situ surface-enhanced infrared absorption spectroscopy (SEIRAS) to investigate the impact of the bonding environment of Pd on the EOR performance over NHEA@NHEA-Pd and Sn@Sn-Pd (Figure 4d,e). The main feature observed in the SEIRAS with the potential range of 0.1–0.9 V versus RHE on the two catalysts can be attributed to CO adsorbed in a bridge configuration within 1794–1819 cm^{-1}.[81] For the NHEA@NHEA-Pd catalyst (Figure 4d), a CO adsorption band was observed at 1794 cm^{-1} when testing at 0.1 V versus RHE, suggesting that activations of C-H and C-C bonds in the EOR were relatively facile. The intensity of the CO band increases as the potential rises to 0.5 V versus RHE, indicating that CO accumulates on the catalyst surface via ethanol activation but cannot be effectively removed by its oxidation. Concomitantly, the band blueshifts to 1827 cm^{-1} owing to both the vibrational Stark effect[82] and the dynamical dipole coupling.[83] As the potential rises from 0.5 to 0.9 V versus RHE, the CO adsorbed band redshifts and its corresponding intensity gradually diminishes. While the vibrational Stark effect is expected to lead to further blueshifts, its effect is more than offset by the reduced dynamical dipole coupling due to the decreased CO coverage. Thus, the potential at which the CO adsorption band starts to redshift as potential becomes more positive can be interpreted as the onset of the CO oxidation, which is 0.5 V versus RHE on NHEA@NHEA-Pd. In contrast, the CO oxidation commences at 0.7–0.8 V versus RHE on Sn@Sn-Pd, which is a clear indication that Pd in NHEA@NHEA-Pd is more efficient in oxidizing CO than Sn@Sn-Pd (Figure 4e,f). Moreover, the in situ study also confirms that NHEA@NHEA-Pd has excellent anti-CO poison capabilities (by catalytic removal).

The above in situ experiments also confirm the conversion of ethanol to CO during the catalytic reaction (>0.1 V vs RHE) which gradually oxidized into CO_2 when the potential increases above 0.5 V. To further demonstrate the production of CO_2 and the complete 12 electron process on HEA catalysts, we used the titration method[56] to determine the content of CO_3^{2-}, which is generated from the reaction between the CO_2 and OH^- in the alkaline solution. As shown in Figure S23, Supporting Information, after adding $Ba(OH)_2$ $8H_2O$, the solution from NHEA@NHEA-Pd becomes more turbid and has precipitate coagulation, which proves that it produces more CO_3^{2-} (or CO_2) after the chronoamperometric test (0.8 V, 2 h). The titration experiment confirms the existence of CO_2 during EOR and a complete 12-electron transfer process over HEA catalysts.

Based on the above electrochemical measurements, the NHEA@NHEA-Pd shows better performance than Sn@Sn-Pd both in terms of catalytic activity and CO tolerance, which strongly indicates the importance of Pd's coordination environment to affect its performances. Notably, we find clear performance differences when Pd is in different coordination environments (Figure 4g): commercial Pd (Pd-Pd), Sn@Sn-Pd (Pd-Sn), and NHEA@NHEA-Pd (Pd-NHEA), by comparing the specific activities (normalizing by ECSA) which is

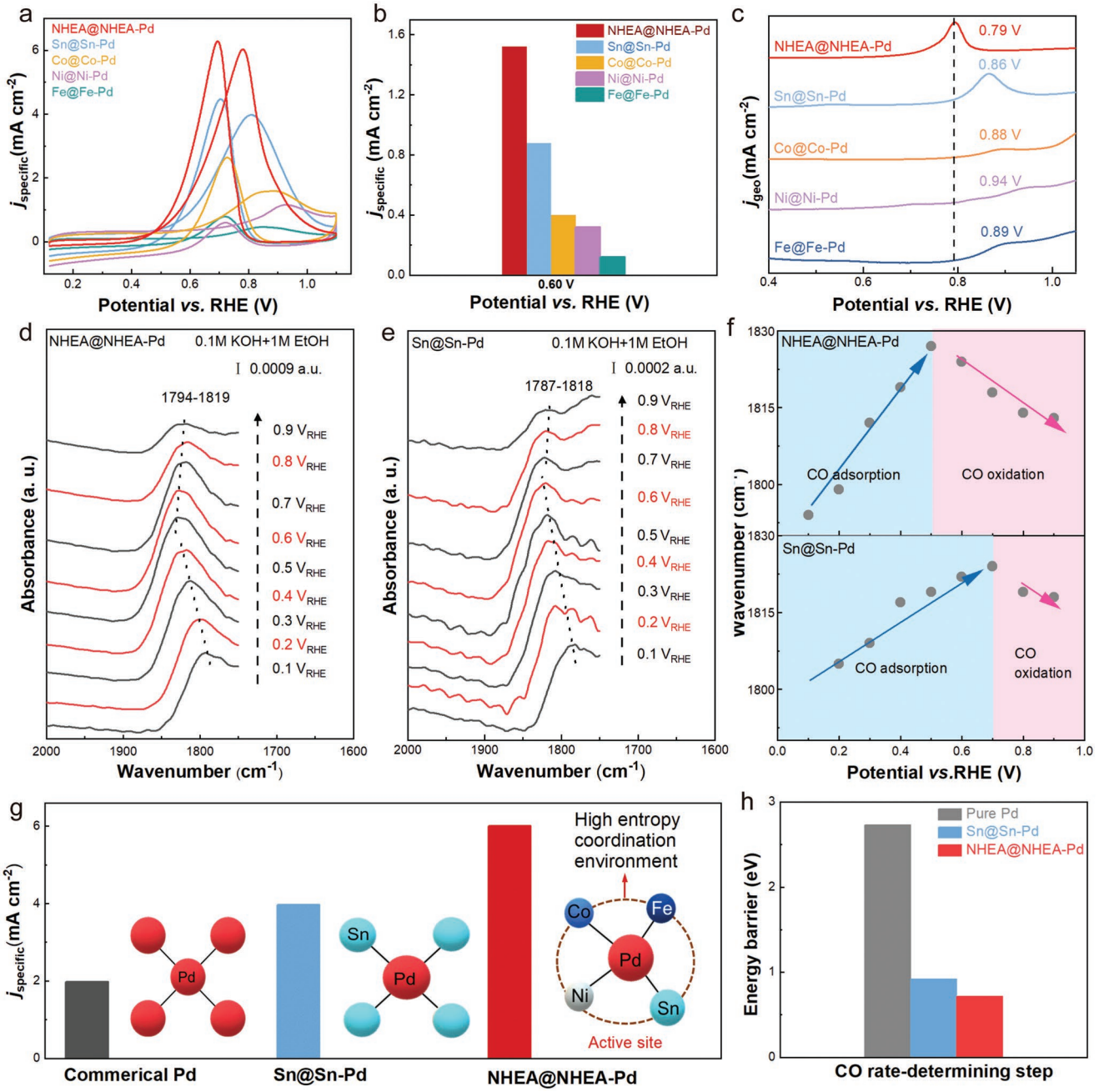

Figure 4. Origin of high performance on the NHEA@NHEA-Pd catalyst. a,b) Specific activities of NHEA@NHEA-Pd and M@M-Pd in EOR. c) CO stripping test for NHEA@NHEA-Pd versus M@M-Pd, where NHEA@NHEA-Pd displays the lowest onset potential and thus indicates higher activity and better anti-CO poison effect. d,e) In situ SEIRAS study of EOR on NHEA@NHEA-Pd and Sn@Sn-Pd, where NHEA@NHEA-Pd shows 0.3 V lower onset potential for CO oxidation (f), namely high intrinsic activity. g) Specific activity comparison among Pd, Sn@Sn-Pd, and NHEA@NHEA-Pd, showing the important role of coordination environments on the activity of Pd. h) DFT study of CO oxidation on three different Pd's coordination environments (Pd-Pd, Pd-Sn, and Pd-NHEA), where NHEA-Pd shows the lowest energy barrier.

an indication of intrinsic activity. To understand the influence of the high-entropy coordination environment on the Pd's activity, we studied the EOR performance by density functional theory (DFT) calculations on three coordination environments (Pd-Pd, Pd-Sn, and Pd-NHEA, see the Experimental Section and Figure S24, Supporting Information). We specifically focused on the CO oxidation step since it was experimentally confirmed by our in situ study and is widely considered the main poisoning intermediate leading to performance degradation.[84] As shown in Figure 4h, Pd shows a much higher energy barrier (2.72 eV) while NHEA@NHEA-Pd has the lowest energy barrier (0.72 eV) for CO oxidation, thus facilitating the catalytic CO oxidation and removing (anti-CO poison) with both high activity and stability, also imply the overall high activity and stability in EOR.

Therefore, from the catalytic performance, CO stripping test, in situ spectroscopy study, and theoretical calculations, it can be concluded that the high performance of NHEA@NHEA-Pd mostly comes from the following aspects: 1) our surface decoration enables highly dispersed and exposed surface Pd with more effective active sites, as compared with solid-solution NHEA-Pd and pure Pd having buried Pd; 2) the Pd's high-entropy coordination environment effectively modulate the performance of Pd and lowers the reaction energy barrier for EOR, which promotes enhanced intrinsic activity as compared with Pd and Sn@Sn-Pd; and 3) the high-entropy structure also stabilize Pd for a durable performance owing to the entropy stabilization effect.[18,20,85]

3. Conclusion

In summary, we develop a two-step thermal shock process to achieve surface decoration of HEA catalysts to drastically improve their activity and stability, as well as significantly reduce cost, as demonstrated in the model reaction of EOR. The NHEA@NHEA-Pd exhibits a high mass activity of 7.34 A mg^{-1}_{Pd} and excellent stability (8.2% loss after 2000 cycles), which is significantly better than commercial Pd/C or solid-solution NHEA-Pd. Compared with individual M@M-Pd, NHEA@NHEA-Pd outperforms all of them in terms of activity and stability. The high-performance NHEA@NHEA-Pd is a combined result of 1) highly dispersed and exposed active sites by the surface decoration, 2) enhanced intrinsic activity of Pd having the unique high-entropy coordination environment, and 3) entropy stabilization for improved stability. The high-entropy structure shows great promise for the cascade reactions where different optimal binding energies can be provided by different binding groups correlated to different element-based sites. Therefore, our work provides a highly efficient route to design high-performing catalysts by combining surface decoration and high-entropy modulation, which can simultaneously achieve boosted activity, stability, as well as reduced cost. These multielement catalysts are especially suitable for a range of complex multi-step reactions requiring multifunctional active sites such as alcohol oxidation, CO_2 reduction, and Nitrogen (N_2) fixation.

4. Experimental Section

Material Preparation: The metal salts such as palladium chloride, tin chloride, iron (III) chloride, cobalt chloride hexahydrate, nickel chloride hexahydrate, and commercial 10.0 wt% Pd/C were purchased from Aladdin. Commercial carbon black (Vulcan XC72R, Cabot) was utilized as the substrate. The precursor solution (0.05 mol L^{-1}) was prepared by dissolving various metal salts with an equimolar concentration in ethanol. The mixed non-noble metal solution was added into carbon black with a targeted loading concentration, and then sonicated for 2 h. The mixture was dried in a vacuum drying oven to achieve precursor-loaded carbon black. A two-step thermal shock procedure was used to synthesize the catalysts. The obtained powders were subjected to high-temperature shock by a commercial carbon cloth heating element driven by a DC power supply (MR50040, BK PRECISION). The corresponding temperature was captured by an Endurance IR camera (E1RH-R59-V-0-0) with a temperature resolution of ±2 K and a response time of 10 ms.

Materials Characterization: A diffractometer (XRD 700D, Shimadzu Corporation, Japan) was used to characterize the XRD of the catalyst at room temperature. XPS data of NHEA@NHEA-Pd and Sn@Sn-Pd were collected using an AXIS-ULTRA DLD-600W (Kratos, Japan). The mass was determined by inductively coupled plasma optical emission spectroscopy (ICP-OES), and the mass loading of each metal element in NHEA@NHEA-Pd on carbon black was 0.443 wt% for Pd, 1.21 wt% for Sn, 1.88 wt% for Co, and 1.93 wt% for Ni, which was close to the designed loading. The morphology of the catalysts was examined by a JEOL 2100 TEM at the acceleration voltage of 200 kV. HRTEM and HAADF-STEM images were performed on a Talos F200X with a probe spherical aberration corrector at an operation voltage of 300 kV.

Electrocatalytic Tests: A three-electrode system connected with CHI 760 electrochemical workstation was used for the test. A glassy carbon (5 mm in diameter) was used as the working electrode. The counter electrode was the Pt sheet and the reference electrode was the calomel (saturated KCl) or Ag/AgCl: (saturated KCl). The electrolytes of 0.5 M H_2SO_4 and 1 M KOH with 1 M ethanol or without ethanol were used. In terms of electrode preparation, 5 mg catalysts were dispersed in 1 mL solution composed of water (200 µL), isopropanol (800 µL), and 5.0 wt% Nafion (20 µL) and then sonicated for 30 min. The as-prepared ink 10 µL was dropped onto the glassy carbon for the working electrode, and further dried at room temperature. The potentials were converted to that versus RHE according to the Nernst equation ($E_{RHE} = E_{Ag/AgCl} + 0.0591\ pH + 0.197$) for Ag/AgCl and the Nernst equation ($E_{RHE} = E_{calomel} + 0.0591\ pH + 0.242$) for calomel. All electrolytes were purged with N_2 for 30 min. For the ECSA test, all the catalysts were activated by potential cycling from 0.01 to 1.10 V (vs RHE) in a 0.5 M H_2SO_4 solution with a scan rate of 200 mV s^{-1} for several hundred cycles until reaching a stable CV curve. For the ECSA, the catalysts were scanned in the same region and electrolyte but at a low sweep rate such as 20 mV s^{-1}. The ECSA ($m^2\ g^{-1}pd$) is defined as follows:

$$ECSA = Q/\left(0.405 \times W_{pd}\right) \tag{1}$$

where Q corresponds to the reduced charge of PdO (mC), 0.405 is the charge required to reduce a monolayer of PdO (mC cm^{-2}_{Pd}), and W_{Pd} represents the amount of Pd (mg cm^{-2}) loaded on the GCE.

For the EOR, the CVs were recorded in a 1 M KOH solution with 1 M ethanol at the potential from 0.01 to 1.10 V (vs RHE). The sweep rate was fixed at 20 mV s^{-1}. CA analysis was performed at 0.45 V (vs RHE). For the CO stripping, first, the catalysts underwent electrochemical pre-treatment by potential cycling between 0.01 and 1.20 V for multiple cycles at a scan rate of 200 mV s^{-1} under an N_2-saturated 1.0 M KOH electrolyte. Then, two CVs cycling between 0.05 and 1.05 V were recorded at 20 mV s^{-1}. Next, the working electrode was maintained in a CO-saturated solution for 20 min. Afterward, two additional CVs were measured between 0.01 and 1.20 V with a scan rate of 20 mV s^{-1} in an N_2-saturated solution.

CO_2 Detection and Selectivity Estimation: To further demonstrate the production of CO_2, the titration method was used to determine the content of CO_3^{2-} which was generated from the reaction between the CO_2 and OH^- in the alkaline solution.

Experimental Procedure for CO_2 Detection: It was assumed that 12- and 4-electron pathways produced CO_2 and acetate, respectively. Particularly, the 12-electron ($12e^-$) pathway in alkaline solution was the following:

$$CH_3CH_2OH + 16OH^- \rightarrow 2CO_3^{2-} + 11H_2O + 12e^- \tag{2}$$

$Ba(OH)_2\ 8H_2O$ was used to react with CO_3^{2-} to generate precipitation of $BaCO_3$ and the amount of CO_2 generated from EOR could be measured by weighing the precipitate.

$$CO_3^{2-} + Ba^{2+} \rightarrow BaCO_3\,(\text{precipitation}) \tag{3}$$

To prevent contamination of CO_2 from the air, the experiments were performed in a sealed and air-free H-type cell with continuous N_2 gas flowing into 100 mL electrolyte (1 M KOH + 1 M ethanol). After the

chronoamperometric test (0.8 V vs RHE) for 2 h, 30 mL electrolyte was used for titration. Excessive barium hydroxide ($Ba(OH)_2$ 8H2O, 1 M, Alfa, 98%) was added to the electrolyte, and white $BaCO_3$ precipitation was collected.

SEIRAS Method—Materials: The Au film was pre-deposited directly on a Si prism by chemical deposition method as reported in a previous report.[86] NHEA@NHEA-Pd and Sn@Sn-Pd were deposited on the Au film applying the method outlined by Heyes et al.[87]

SEIRAS Method—Spectroscopic Experiments: An anion exchange membrane-separated two-compartment, three-electrode spectroelectrochemical stirred cell as decried in previous reports[88,89] was used for the in situ SEIRAS tests. The cell was integrated into a Bruker FT-IR Spectrometer INVENIO equipped with a liquid nitrogen-cooled mercury cadmium telluride detector. All spectra were collected at a 4 cm^{-1} spectral resolution and were presented in absorbance units. The potential on the cell was supplied by the Biologic VSP system for electrochemical measurements. Before collecting the spectra, the background was taken at open circuit potential in Ar-saturated 0.1 M KOH containing 1 M ethanol. The forward and backward scanning at 5 mV s^{-1} were tested, proving the feasibility of the in situ SEIRAS study (Figures S20–S22, Supporting Information).

Density Functional Theory Calculation—Methods: All spin-polarized DFT calculations were performed using Vienna Ab initio Simulation Package (VASP). The projector-augmented wave method and Perdew–Burke–Ernzerhof functional were used. The Kohn–Sham wave functions were expanded in a plane-wave basis set with a cutoff energy of 500 eV. The Brillouin zone was sampled by the $2 \times 2 \times 1$ Monkhorst–Pack k-point mesh. Period boundary conditions were applied in both in-plane and interlayer directions. A vacuum region of 15 Å was created to ensure negligible interaction between mirror images. 12.48 Å × 12.87 Å cubic supercells were built. All atoms in this system were allowed to relax until the forces fell below 0.02 eV $Å^{-1}$. The reaction free energy ΔG was defined as the difference between free energies of the initial and final states as calculated by the equation.

$$\Delta G = \Delta E + \Delta ZPE - T\Delta S + \Delta G_U + \Delta G_{pH} \quad (4)$$

where ΔE is the total energy difference between reactants and products of reactions; ΔZPE is the zero-point energy correction; ΔS is the vibrational entropy change at finite temperature T. ΔG_U is equal to $-eU$, where e is the elementary charge; U is the electrode potential; ΔG_{pH} is the correction of the H^+ free energy. $\Delta G_{pH} = -k_B T \ln[H^+] = k_B T \mathrm{pH} \ln 10 = 0.0591$ pH, where k_B is the Boltzmann constant; T is the temperature and pH was 14.

Statistical Analysis: At least ten samples were tested for each catalyst in the electrocatalytic tests. All graphs were plotted by Origin 2020. The size of nanoparticles was calculated using Image J for TEM images. XPS results were fitted to deconvolve the peaks using Avantage.

Supporting Information

Supporting Information is available from the Wiley Online Library or from the author.

Acknowledgements

Y.Y. was supported by the National Key R&D Program of China (2021YFA1202300), the National Natural Science Foundation of China (No. 52101255), and the Fundamental Research Funds for the Central Universities, HUST: 5003110114, 0214110106. Z.L. acknowledges the support by the Suzhou Key Laboratory of Functional Nano & Soft Materials, Collaborative Innovation Center of Suzhou Nano Science & Technology, and the 111 Project. W.G., Z.L., J.Z., and B.X. acknowledge the support of the Beijing National Laboratory for Molecular Sciences. L.W. and T.L. acknowledge the University of Maryland supercomputing resources (http://hpcc.umd.edu) and Maryland Advanced Research Computing Center (MARCC) for conducting the research reported in this paper. The authors thank the help from Huazhong University of Science & Technology Analytical Center.

Conflict of Interest

The authors declare no conflict of interest.

Data Availability Statement

Research data are not shared.

Keywords

entropy stabilization, ethanol oxidation reactions, high-entropy alloy catalysts, high-entropy coordination environments, surface decorations

Received: April 25, 2022
Revised: May 14, 2022
Published online: June 2, 2022

[1] Y. Yao, Q. Dong, A. Brozena, J. Luo, J. Miao, M. Chi, C. Wang, A. Anapolsky, L. Hu, *Science* **2022**, *376*, 3103.
[2] E. P. George, D. Raabe, R. O. Ritchie, *Nat. Rev. Mater.* **2019**, *4*, 515.
[3] S. Gao, S. Hao, Z. Huang, Y. Yuan, S. Han, L. Lei, X. Zhang, R. Shahbazian-Yassar, J. Lu, *Nat. Commun.* **2020**, *11*, 2016.
[4] T. A. A. Batchelor, J. K. Pedersen, S. H. Winther, I. E. Castelli, K. W. Jacobsen, J. Rossmeisl, *Joule* **2019**, *3*, 834.
[5] A. Amiri, R. Shahbazian-Yassar, *J. Mater. Chem. A* **2021**, *9*, 782.
[6] Y. Yao, Z. Huang, P. Xie, S. D. Lacey, R. J. Jacob, H. Xie, F. Chen, A. Nie, T. Pu, M. Rehwoldt, D. Yu, M. R. Zachariah, C. Wang, R. Shahbazian-Yassar, J. Li, L. Hu, *Science* **2018**, *359*, 1489.
[7] T. Löffler, A. Ludwig, J. Rossmeisl, W. Schuhmann, *Angew. Chem. Int. Ed.* **2021**, *60*, 26894.
[8] W.-T. Koo, J. E. Millstone, P. S. Weiss, I.-D. Kim, *ACS Nano* **2020**, *14*, 6407.
[9] D. Wu, K. Kusada, Y. Nanba, M. Koyama, T. Yamamoto, T. Toriyama, S. Matsumura, O. Seo, I. Gueye, J. Kim, L. S. R. Kumara, O. Sakata, S. Kawaguchi, Y. Kubota, H. Kitagawa, *J. Am. Chem. Soc.* **2022**, *144*, 3365.
[10] D. Wu, K. Kusada, T. Yamamoto, T. Toriyama, S. Matsumura, I. Gueye, O. Seo, J. Kim, S. Hiroi, O. Sakata, S. Kawaguchi, Y. Kubota, H. Kitagawa, *Chem. Sci.* **2020**, *11*, 12731.
[11] N. Zhou, T. Hu, J. Huang, J. Luo, *Scr. Mater.* **2016**, *124*, 160.
[12] S. A. Kube, J. Schroers, *Scr. Mater.* **2020**, *186*, 392.
[13] B. Song, Y. Yang, M. Rabbani, T. T. Yang, K. He, X. Hu, Y. Yuan, P. Ghildiyal, V. P. Dravid, M. R. Zachariah, W. A. Saidi, Y. Liu, R. Shahbazian-Yassar, *ACS Nano* **2020**, *14*, 15131.
[14] Y. Yao, Z. Liu, P. Xie, Z. Huang, T. Li, D. Morris, Z. Finfrock, J. Zhou, M. Jiao, J. Gao, Y. Mao, J. Miao, P. Zhang, R. Shahbazian-Yassar, C. Wang, G. Wang, L. Hu, *Sci. Adv.* **2020**, *6*, eaaz0510.
[15] S. D. Lacey, Q. Dong, Z. Huang, J. Luo, H. Xie, Z. Lin, D. J. Kirsch, V. Vattipalli, C. Povinelli, W. Fan, R. Shahbazian-Yassar, D. Wang, L. Hu, *Nano Lett.* **2019**, *19*, 5149.
[16] D. B. Miracle, O. N. Senkov, *Acta Mater.* **2017**, *122*, 448.
[17] R. Guo, L. Yu, Z. Liu, J. Pan, Y. Yao, L. Liu, *Nano Res.* **2021**, 1.
[18] T. Li, Y. Yao, Z. Huang, P. Xie, Z. Liu, M. Yang, J. Gao, K. Zeng, A. H. Brozena, G. Pastel, M. Jiao, Q. Dong, J. Dai, S. Li, H. Zong,

M. Chi, J. Luo, Y. Mo, G. Wang, C. Wang, R. Shahbazian-Yassar, L. Hu, *Nat. Catal.* **2021**, *4*, 62.
[19] T. Löffler, A. Savan, H. Meyer, M. Meischein, V. Strotkötter, A. Ludwig, W. Schuhmann, *Angew. Chem. Int. Ed.* **2020**, *59*, 5844.
[20] T. Li, Q. Dong, Z. Huang, L. Wu, Y. Yao, J. Gao, X. Wang, H. Zhang, D. Wang, T. Li, R. Shahbazian-Yassar, L. Hu, *Adv. Mater.* **2022**, *34*, 2106436.
[21] P. Xie, Y. Yao, Z. Huang, Z. Liu, J. Zhang, T. Li, G. Wang, R. Shahbazian-Yassar, L. Hu, C. Wang, *Nat. Commun.* **2019**, *10*, 4011.
[22] F. Chen, Y. Yao, A. Nie, S. Xu, J. Dai, E. Hitz, Y. Li, A. Lu, Z. Huang, T. Li, R. Shahbazian-Yassar, L. Hu, *Adv. Energy Mater.* **2018**, *8*, 1800466.
[23] Z. Jia, T. Yang, L. Sun, Y. Zhao, W. Li, J. Luan, F. Lyu, L. C. Zhang, J. J. Kruzic, J. J. Kai, J. C. Huang, J. Lu, C. T. Liu, *Adv. Mater.* **2020**, *32*, 2070166.
[24] W. Shi, H. Liu, Z. Li, C. Li, J. Zhou, Y. Yuan, F. Jiang, K. K. Fu, Y. Yao, *SusMat* **2022**, *2*, 186.
[25] S. Nellaiappan, N. Kumar, R. Kumar, A. Parui, K. D. M. Alviya, K. G. Pradeep, A. K. Singh, S. Sharma, C. S. Tiwary, K. Biswas, *chemrxiv.9777218.v1. ChemRxiv* **2019**, https://chemrxiv.org/articles/Nobel_Metal_Based_High_Entropy_Alloy_for_Conversion_of_Carbon_Dioxide_CO2_to_Hydrocarbon/9777218.
[26] J. K. Pedersen, T. A. A. Batchelor, A. Bagger, J. Rossmeisl, *ACS Catal.* **2020**, *10*, 2169.
[27] K. V. Yusenko, S. Riva, P. A. Carvalho, M. V. Yusenko, S. Arnaboldi, A. S. Sukhikh, M. Hanfland, S. A. Gromilov, *Scr. Mater.* **2017**, *138*, 22.
[28] S. Li, J. Wang, X. Lin, G. Xie, Y. Huang, X. Liu, H. J. Qiu, *Adv. Funct. Mater.* **2021**, *31*, 2007129.
[29] D. Wu, K. Kusada, T. Yamamoto, T. Toriyama, S. Matsumura, S. Kawaguchi, Y. Kubota, H. Kitagawa, *J. Am. Chem. Soc.* **2020**, *142*, 13833.
[30] Q. Wang, L. Velasco, B. Breitung, V. Presser, *Adv. Energy Mater.* **2021**, *11*, 2102355.
[31] C. R. McCormick, R. E. Schaak, *J. Am. Chem. Soc.* **2021**, *143*, 1017.
[32] D. Zhang, H. Zhao, X. Wu, Y. Deng, Z. Wang, Y. Han, H. Li, Y. Shi, X. Chen, S. Li, J. Lai, B. Huang, L. Wang, *Adv. Funct. Mater.* **2021**, *31*, 2006939.
[33] H. Liu, L. Syama, L. Zhang, C. Lee, C. Liu, Z. Dai, Q. Yan, *SusMat* **2021**, *1*, 482.
[34] Y. Sun, S. Dai, *Sci. Adv.* **2021**, *7*, eabg1600.
[35] Y. Yao, Z. Huang, T. Li, H. Wang, Y. Liu, H. S. Stein, Y. Mao, J. Gao, M. Jiao, Q. Dong, J. Dai, P. Xie, H. Xie, S. D. Lacey, I. Takeuchi, J. M. Gregoire, R. Jiang, C. Wang, A. D. Taylor, R. Shahbazian-Yassar, L. Hu, *Proc. Natl. Acad. Sci. U. S. A.* **2020**, *117*, 6316.
[36] Z. Lu, Z. W. Chen, C. V. Singh, *Matter* **2020**, *3*, 1318.
[37] Y. C. Han, M. L. Liu, L. Sun, X. C. Li, Y. Yao, C. Zhang, S. Y. Ding, H. G. Liao, L. Zhang, F. R. Fan, M. Moskovits, Z. Q. Tian, *Nano Energy* **2022**, *97*, 107125.
[38] J. Feng, D. Chen, P. V. Pikhitsa, Y. Jung, J. Yang, M. Choi, *Matter* **2020**, *3*, 1646.
[39] H. Li, J. Lai, Z. Li, L. Wang, *Adv. Funct. Mater.* **2021**, *31*, 2106715.
[40] M. Fu, X. Ma, K. Zhao, X. Li, D. Su, *iScience* **2021**, *24*, 102177.
[41] Y. Chen, H. Fu, Y. Huang, L. Huang, X. Zheng, Y. Dai, Y. Huang, W. Luo, *ACS Mater. Lett.* **2021**, *3*, 160.
[42] Y. Ma, Y. Ma, Q. Wang, S. Schweidler, M. Botros, T. Fu, H. Hahn, T. Brezesinski, B. Breitung, *Energy Environ. Sci.* **2021**, *14*, 2883.
[43] Y. Wang, X. Zheng, D. Wang, *Nano Res.* **2022**, *15*, 1730.
[44] J. Linnemann, K. Kanokkanchana, K. Tschulik, *ACS Catal.* **2021**, *11*, 5318.
[45] H. J. Qiu, G. Fang, Y. Wen, P. Liu, G. Xie, X. Liu, S. Sun, *J. Mater. Chem. A* **2019**, *7*, 6499.
[46] J. N. Tiwari, S. Sultan, C. W. Myung, T. Yoon, N. Li, M. Ha, A. M. Harzandi, H. J. Park, D. Y. Kim, S. S. Chandrasekaran, W. G. Lee, V. Vij, H. Kang, T. J. Shin, H. S. Shin, G. Lee, Z. Lee, K. S. Kim, *Nat. Energy* **2018**, *3*, 773.
[47] X. Tian, X. Zhao, Y. Q. Su, L. Wang, H. Wang, D. Dang, B. Chi, H. Liu, E. J. M. Hensen, X. W. Lou, B. Y. Xia, *Science* **2019**, *366*, 850.
[48] Z. Jin, J. Lyu, Y. L. Zhao, H. Li, Z. Chen, X. Lin, G. Xie, X. Liu, J. J. Kai, H. J. Qiu, *Chem. Mater.* **2021**, *33*, 1771.
[49] H. Xie, S. Chen, J. Liang, T. Wang, Z. Hou, H. L. Wang, G. Chai, Q. Li, *Adv. Funct. Mater.* **2021**, *31*, 2100883.
[50] M. Wu, M. Cui, L. Wu, S. Hwang, C. Yang, Q. Xia, G. Zhong, H. Qiao, W. Gan, X. Wang, D. Kline, M. R. Zachariah, D. Su, T. Li, L. Hu, *Adv. Energy Mater.* **2020**, *10*, 20.
[51] L. Wang, Z. Zeng, W. Gao, T. Maxson, D. Raciti, M. Giroux, X. Pan, C. Wang, J. Greeley, *Science* **2019**, *363*, 870.
[52] G. Doubek, R. C. Sekol, J. Li, W. H. Ryu, F. S. Gittleson, S. Nejati, E. Moy, C. Reid, M. Carmo, M. Linardi, P. Bordeenithikasem, E. Kinser, Y. Liu, X. Tong, C. O. Osuji, J. Schroers, S. Mukherjee, A. D. Taylor, *Adv. Mater.* **2016**, *28*, 1940.
[53] B. B. Rajeeva, P. Kunal, P. S. Kollipara, P. V. Acharya, M. Joe, M. S. Ide, K. Jarvis, Y. Liu, V. Bahadur, S. M. Humphrey, Y. Zheng, *Matter* **2019**, *1*, 1606.
[54] H. L. Liu, F. Nosheen, X. Wang, *Chem. Soc. Rev.* **2015**, *44*, 3056.
[55] D. Jiang, Y. Yao, T. Li, G. Wan, X. I. Pereira-Hernández, Y. Lu, J. Tian, K. Khivantsev, M. H. Engelhard, C. Sun, C. E. García-Vargas, A. S. Hoffman, S. R. Bare, A. K. Datye, L. Hu, Y. Wang, *Angew. Chem. Int. Ed.* **2021**, *60*, 26054.
[56] J. Chang, G. Wang, M. Wang, Q. Wang, B. Li, H. Zhou, Y. Zhu, W. Zhang, M. Omer, N. Orlovskaya, Q. Ma, M. Gu, Z. Feng, G. Wang, Y. Yang, *Nat. Energy* **2021**, *6*, 1144.
[57] X. Yang, Z. Liang, S. Chen, M. Ma, Q. Wang, X. Tong, Q. Zhang, J. Ye, L. Gu, N. Yang, *Small* **2020**, *16*, 2004727.
[58] P. F. Yin, M. Zhou, J. Chen, C. Tan, G. Liu, Q. Ma, Q. Yun, X. Zhang, H. Cheng, Q. Lu, B. Chen, Y. Chen, Z. Zhang, J. Huang, D. Hu, J. Wang, Q. Liu, Z. Luo, Z. Liu, Y. Ge, X. J. Wu, X. W. Du, H. Zhang, *Adv. Mater.* **2020**, *32*, 2000482.
[59] X. Li, H. Rong, J. Zhang, D. Wang, Y. Li, *Nano Res.* **2020**, *13*, 1842.
[60] Y. Zhu, J. Sokolowski, X. Song, Y. He, Y. Mei, G. Wu, *Adv. Energy Mater.* **2020**, *10*, 1902844.
[61] Y. Qiao, Y. Liu, Y. Liu, Q. Dong, G. Zhong, X. Wang, Z. Liu, X. Wang, S. He, W. Zhou, G. Wang, C. Wang, L. Hu, *Small Methods* **2020**, *4*, 2000265.
[62] W. Du, K. E. MacKenzie, D. F. Milano, N. A. Deskins, D. Su, X. Teng, *ACS Catal.* **2012**, *2*, 287.
[63] L. Nahar, A. A. Farghaly, R. J. A. Esteves, I. U. Arachchige, *Chem. Mater.* **2017**, *29*, 7704.
[64] W. Huang, X. Y. Ma, H. Wang, R. Feng, J. Zhou, P. N. Duchesne, P. Zhang, F. Chen, N. Han, F. Zhao, J. Zhou, W. Bin Cai, Y. Li, *Adv. Mater.* **2017**, *29*, 1703057.
[65] L. Chen, L. Lu, H. Zhu, Y. Chen, Y. Huang, Y. Li, L. Wang, *Nat. Commun.* **2017**, *8*, 14136.
[66] Y. J. Chen, Y. R. Chen, C. H. Chiang, K. L. Tung, T. K. Yeh, H. Y. Tuan, *Nanoscale* **2019**, *11*, 3336.
[67] Y. Zhu, L. Bu, Q. Shao, X. Huang, *ACS Catal.* **2019**, *9*, 6607.
[68] M. Zhou, J. Liu, C. Ling, Y. Ge, B. Chen, C. Tan, Z. Fan, J. Huang, J. Chen, Z. Liu, Z. Huang, J. Ge, H. Cheng, Y. Chen, L. Dai, P. Yin, X. Zhang, Q. Yun, H. Zhang, *Adv. Mater.* **2021**, *34*, 2106115.
[69] T. Li, Y. Yao, B. H. Ko, Z. Huang, Q. Dong, J. Gao, W. Chen, J. Li, S. Li, X. Wang, R. Shahbazian-Yassar, F. Jiao, L. Hu, *Adv. Funct. Mater.* **2021**, *31*, 2010561.
[70] Y. Yao, Z. Zhang, L. Jiao, *Energy Environ. Mater.* **2022**, *5*, 470.
[71] H. Lv, Y. Wang, A. Lopes, D. Xu, B. Liu, *Appl. Catal. B Environ.* **2019**, *249*, 116.
[72] M. Zareie Yazdan-Abad, M. Noroozifar, N. Alfi, A. R. Modarresi-Alam, H. Saravani, *Int. J. Hydrogen Energy* **2018**, *43*, 12103.
[73] A. Shafaei Douk, H. Saravani, M. Noroozifar, *Electrochim. Acta* **2018**, *275*, 182.
[74] Y. Wang, W. Wang, F. Xue, Y. Cheng, K. Liu, Q. Zhang, M. Liu, S. Xie, *Chem. Commun.* **2018**, *54*, 5185.

[75] Z. Liang, L. Song, S. Deng, Y. Zhu, E. Stavitski, R. R. Adzic, J. Chen, J. X. Wang, *J. Am. Chem. Soc.* **2019**, *141*, 9629.
[76] M. Smiljanić, M. Bele, L. Moriau, F. Ruiz-Zepeda, M. Šala, N. Hodnik, *J. Phys. Chem. C* **2021**, *125*, 27534.
[77] Y. Qiu, J. Zhang, J. Jin, J. Sun, H. Tang, Q. Chen, Z. Zhang, W. Sun, G. Meng, Q. Xu, Y. Zhu, A. Han, L. Gu, D. Wang, Y. Li, *Nat. Commun.* **2021**, *12*, 5273.
[78] D. Liu, Q. Zeng, H. Liu, C. Hu, D. Chen, L. Xu, J. Yang, *Cell Rep. Phys. Sci.* **2021**, *2*, 100357.
[79] X. Ao, W. Zhang, B. Zhao, Y. Ding, G. Nam, L. Soule, A. Abdelhafiz, C. Wang, M. Liu, *Energy Environ. Sci.* **2020**, *13*, 3032.
[80] S. Lee, J. H. Jang, I. Jang, D. Choi, K. S. Lee, D. Ahn, Y. S. Kang, H. Y. Park, S. J. Yoo, *J. Catal.* **2019**, *379*, 112.
[81] S. Pronkin, T. Wandlowski, *Surf. Sci.* **2004**, *573*, 109.
[82] E. Borguet, H. L. Dai, *J. Chem. Phys.* **1994**, *101*, 9080.
[83] M. J. Weaver, *Appl. Surf. Sci.* **1993**, *67*, 147.
[84] J. Bai, X. Xiao, Y. Y. Xue, J. X. Jiang, J. H. Zeng, X. F. Li, Y. Chen, *ACS Appl. Mater. Interfaces* **2018**, *10*, 19755.
[85] Y. C. Yang, C. Liu, C. Y. Lin, Z. Xia, *Scr. Mater.* **2020**, *178*, 181.
[86] M. Dunwell, Q. Lu, J. M. Heyes, J. Rosen, J. G. Chen, Y. Yan, F. Jiao, B. Xu, *J. Am. Chem. Soc.* **2017**, *139*, 3774.
[87] J. Heyes, M. Dunwell, B. Xu, *J. Phys. Chem. C* **2016**, *120*, 17334.
[88] A. S. Malkani, M. Dunwell, B. Xu, *ACS Catal.* **2019**, *9*, 474.
[89] A. S. Malkani, J. Li, J. Anibal, Q. Lu, B. Xu, *ACS Catal.* **2020**, *10*, 941.